# Optically Induced Picosecond Lattice Compression in the Dielectric Component of a Strongly Coupled Ferroelectric/Dielectric Superlattice

*Deepankar Sri Gyan, Hyeon Jun Lee, Youngjun Ahn, Jerome Carnis, Tae Yeon Kim, Sanjith Unithrattil, Jun Young Lee, Sae Hwan Chun, Sunam Kim, Intae Eom, Minseok Kim, Sang-Youn Park, Kyung Sook Kim, Ho Nyung Lee, Ji Young Jo, and Paul G. Evans**

D. Sri Gyan, Dr. H. J. Lee, Dr. Y. Ahn, Prof. P. G. Evans

Department of Materials Science and Engineering, University of Wisconsin-Madison, Madison, Wisconsin 53706, USA

E-mail: pgevans@wisc.edu

Dr. J. Carnis

Aix Marseille Université, Université de Toulon, CNRS, IM2NP, Marseille, France

ESRF - The European Synchrotron, 71 Avenue des Martyrs, 38000 Grenoble, France

Dr. T. Y. Kim, Dr. S. Unithrattil, J. Y. Lee, Prof. J. Y. Jo

School of Materials Science and Engineering, Gwangju Institute of Science and Technology, Gwangju 61005, South Korea

Dr. S. H. Chun, Dr. S. Kim, Dr. I. Eom, Dr. M. Kim, Dr. S. Y. Park, Dr. K. S. Kim

Pohang Accelerator Laboratory, Pohang, Gyeongbuk 37673, South Korea



*This manuscript has been authored by UT-Battelle, LLC under Contract No. DE-AC05-00OR22725 with the U.S. Department of Energy. The United States Government retains and the publisher, by accepting the article for publication, acknowledges that the United States Government retains a non-exclusive, paid-up, irrevocable, world-wide license to publish or reproduce the published form of this manuscript, or allow others to do so, for United States Government purposes. The Department of Energy will provide public access to these results of federally sponsored research in accordance with the DOE Public Access Plan (http://energy.gov/downloads/doe-public-access-plan).*

Dr. H. N. Lee

Materials Science and Technology Division, Oak Ridge National Laboratory, Oak Ridge, Tennessee, 37831, USA

**Keywords:** Ferroelectric/dielectric superlattice, depolarization-field screening, ultrafast structural phenomena, x-ray free-electron laser diffraction

Above-bandgap femtosecond optical excitation of a ferroelectric/dielectric $BaTiO_3/CaTiO_3$ superlattice leads to structural responses that are a consequence of the screening of the strong electrostatic coupling between the component layers. Time-resolved x-ray free-electron laser diffraction shows that the structural response to optical excitation includes a net lattice expansion of the superlattice consistent with depolarization-field screening driven by the photoexcited charge carriers. The depolarization-field-screening driven expansion is separate from a photoacoustic pulse launched from the bottom electrode on which the superlattice was epitaxially grown. The distribution of diffracted intensity of superlattice x-ray reflections indicates that the depolarization-field-screening induced strain includes a photoinduced expansion in the ferroelectric $BaTiO_3$ and a contraction in $CaTiO_3$. The magnitude of expansion in $BaTiO_3$ layers is larger than the contraction in $CaTiO_3$. The difference in the magnitude of depolarization screening driven strain in the $BaTiO_3$ and $CaTiO_3$ components can arise from the contribution of the oxygen octahedral rotation patterns at the $BaTiO_3/CaTiO_3$ interfaces to the polarization of $CaTiO_3$. The depolarization-field-screening driven polarization reduction in the $CaTiO_3$ layers points to a new

direction for the manipulation of polarization in the component layers of a strongly coupled ferroelectric/dielectric superlattice.

## Introduction

Epitaxial superlattice (SL) heterostructures consisting of alternating repeating layers of ferroelectric (FE) and dielectric (DE) complex oxides have polarization configurations that result from a combination of atomic-scale and mesoscopic effects.[1-2] Key effects include the electrostatic coupling between layers, the atomic-scale structure of interfaces, strain arising from the epitaxial mismatch, and the depolarization field arising from the polarization discontinuity at interfaces between FE and DE layers.[3-5] At the nanometer length scale, an internal electric field polarizing the DE layers arises in response to the depolarization field in the FE layer.[6] Structural features such as the octahedral rotation pattern of the component layers can also vary at, and across, interfaces and can affect the equilibrium configuration of the electrical polarization.[2, 7] Non-equilibrium conditions arising after the absorption of an above-band-gap optical pulse further expand the range of phenomena observed in FE/DE SLs. For example, the screening of the depolarization field in SL heterostructures by excited charge carriers leads to transformations between domain configurations and to novel polarization states.[8-13] Charge carriers excited due to the above-bandgap optical excitation of the SL can result in depolarization-field screening, which can reduce the magnitude of the internal electric field polarizing the DE layers. This depolarization field screening driven by optical excitation presents a promising way to modulate the polarization states of the FE/DE SL at an ultrafast timescale. Here, we present a structural study probing the response of a FE/DE SL to a femtosecond optical pulse and find that the optically

induced screening results in a photoinduced lattice compression of the CTO layer.

The equilibrium polarization configuration of FE/DE SLs is determined in large part by the electrostatic interaction between the component layers.[6] The defining issue is that uncompensated charges due to the divergence of the polarization at the FE/DE interface can result in a significant increase in the free energy of the SL.[1] Several possible configurations must be considered as possible routes to reduce relevant free energies. The SL can, for example, adopt a continuous polarization in which there is a decrease in the polarization of the FE layers in comparison with their bulk form and the development of the polarization in the DE layers comparable to that of the FE layers.[14-15] Theoretical studies based on the Landau-Ginzburg-Devonshire (LGD) theory or using density functional theory both predict the emergence of a spontaneous polarization in the DE layer of FE/DE SLs.[6, 16] The octahedral rotation configuration at the FE/DE interfaces can also contribute to the development of electrical polarization in the DE layer.[17]

FE/DE SLs can be broadly categorized as strongly or weakly coupled based on the electrostatic coupling between the ferroelectric layers. SLs with strong electrostatic coupling favor a highly polarized DE layer, rather than the formation of domains or other complex configurations.[6, 15] In contrast, weakly coupled SLs have lower polarization in the DE layers and can exhibit nanodomain and vortex patterns reducing the electrostatic energy that would result from a discontinuity of ferroelectric polarization arising from the creation of an interface between a fully polarized ferroelectric layer and a weakly polarized dielectric layer.[1, 18-20] A dielectric-slab model based on the LGD theory provides a general guideline for the conditions that determine whether a particular SL heterostructure exhibits strong or weak interlayer coupling, with parameters including the relative thickness of the FE and DE layers.[21]

The high concentration of charge carriers resulting from above-bandgap optical excitation changes the local electrostatic conditions by screening the depolarization field.[22-23] The depolarization field screening by optically excited charge carriers can simultaneously increase the polarization of FE layers and reduce the polarization in the DE layers. More specifically, above-bandgap optical excitation can be hypothesized to lead to a high concentration of carriers leading to depolarization-field screening and a subsequent lattice distortion coupled to the polarization of the component layers. This hypothesis is illustrated in **Figure 1(a)**. Changes in the lattice spacing of the BTO and CTO layers respectively, are expected to result from optical excitation. The magnitudes of the change in polarizations of the two layers, $\Delta P_{BTO}$ and $\Delta P_{CTO}$, are not expected to be equal because the polarization of CTO layers does not depend solely on the depolarization field.

In this work, the photoinduced lattice distortion in a strongly coupled $BaTiO_3/CaTiO_3$ (BTO/CTO) SL was probed using ultrafast x-ray free-electron-laser (XFEL) diffraction. The experimental arrangement is shown in **Figure 1(b)**. The SL heterostructure produces several x-ray reflections that include the Bragg reflections arising from the average lattice parameter of the SL and satellite reflections with a wavevector spacing along the surface-normal *z*-direction set by the SL repeating layer thickness. Optically induced structural distortion changes the intensities of the x-ray reflections of the SL, from which the structural changes within the component layers can be determined. The intensities of the SL reflections depend on the relative thicknesses of the BTO and CTO layers and the structure factors of the individual layers and hence can be used to measure the component-specific response.[24-25] The structural responses of the BTO and CTO layers can be determined precisely using a kinematic x-ray diffraction simulation to interpret the observed intensities of the SL x-ray reflections.

The BTO/CTO SL considered here consist of a repeating unit of 2-unit cells (u. c.) of BTO and 4 u. c. of CTO on a $SrRuO_3$ (SRO) bottom electrode on an $SrTiO_3$ (STO) substrate, as illustrated in Figure 1(a) and (b). The SL thin film has an overall thickness of approximately 200 nm. The analysis below considers a model structure consisting of exactly 80 periods corresponding to a thickness $d$=191 nm. SL satellite x-ray reflections are labeled with an integer index $l$, with the 002 SL Bragg reflection at $l$=0, as shown in **Figure 1(c)**. Satellite reflections at higher and lower values of the out-of-plane scattering vector $Q_z$ with respect to the Bragg reflection at $l$=0 have positive and negative values of $l$, respectively. The dielectric slab model predicts that the BTO/CTO SL will exhibit a strong coupling for CTO volume fractions less than a critical value of 33%.[21] Despite having a CTO volume fraction of 67%, larger than the critical value, the 2:4 BTO/CTO SL exhibits strong coupling with nearly equal polarizations of the BTO and CTO layers.[25-26] A precise prediction of the polarization of SLs can be obtained by including the effect of structural reconstruction at interfaces.[2, 17, 27-29] The combined effect of electrical, structural, and mechanical boundary conditions imposed by the superlattice geometry results in a polarization in the CTO layers nearly equal to BTO layers in BTO/CTO SL.[17, 30]

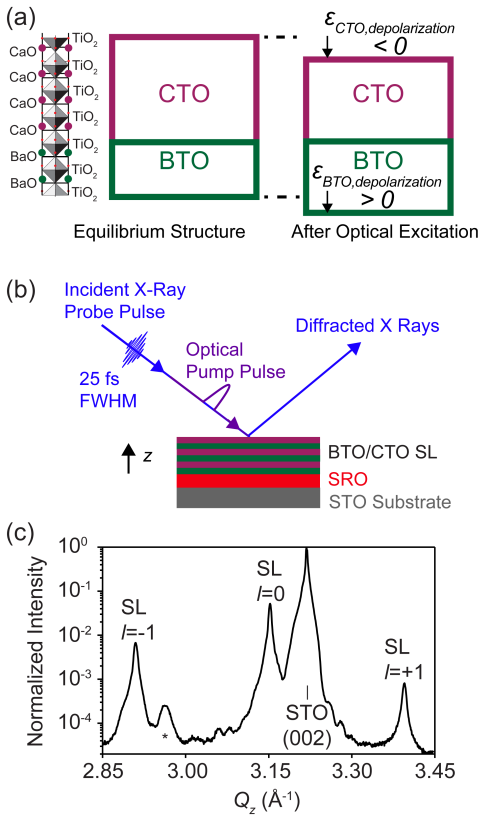


**Figure 1. a)** Atomic arrangement of BTO/CTO SL and schematic of the photoinduced change in the structure arising from the change in the polarization of the component layers. Dashed lines indicate the equilibrium structure before the optical excitation. **b)** Layer structure and experimental arrangement for ultrafast x-ray diffraction study of the optically excited BTO/CTO SL. **c)** Steady-state diffraction pattern acquired with a laboratory x-ray source including the SL *l*=0, +1, and -1 reflections near the 002 Bragg reflection and the STO substrate. The SRO bottom electrode contributes intensity near the STO 002 reflection. An additional reflection from a small fractional component of the thin film is indicated by * and is not considered in the analysis.

**Results and Discussion**

The distortion of the component layers of the SL was determined using the intensities and reciprocal-space locations of the 002 Bragg reflection of the SL, at $l$=0, and the SL satellite reflections with $l$=+1 and $l$=-1. The diffracted x-ray intensities depend on $Q_z$ and on the time interval $t$ between the optical excitation pulse and the x-ray probe pulse. The experimentally measured intensities are shown in **Figure 2a-c**. After optical excitation at $t$=0, each reflection exhibits an initial shift of the diffracted intensity to higher $Q_z$ because of the initial compression of the SL by an acoustic pulse launched from the SRO bottom electrode. At times after 64 ps, there is a shift towards lower $Q_z$, corresponding to a lattice expansion after the propagation of the acoustic pulse into the substrate. A detailed analysis below shows that the responses of the two component layers, however, are different.

The diffraction data in Figure 2 exhibits a series of temporal oscillations of the intensity. The temporal period of the intensity oscillations depends on $\Delta Q_z$, the difference between the value of $Q_z$ and the wavevector of Bragg or SL reflection at each time. The variation of the oscillation period as a function of $\Delta Q_z$ is a signature of the propagation of an acoustic pulse.[13, 31] Analysis of the time dependence of the intensity at the $l$=+1 SL reflection near the 002 reflection and a Fourier analysis of the intensity near this reflection both give a longitudinal sound velocity $v_{SL}$ = 5.9 km $s^{-1}$, as described in the Supporting Information. The acoustic pulse evident in Figure 2 arises because optical absorption heats the conducting SRO layer and establishes a stress profile at $t$=0. The stress in the SRO electrode launches acoustic pulses into the SL and the substrate.[32] The profile and propagation of the strain pulse are discussed in detail in the Supporting Information. The predicted amplitude of the strain pulse due to optical absorption in the SRO layer under the

experimental conditions is 0.7%.

Optical absorption directly in the SL also leads to an increase in its temperature. However, as described in the Supporting Information, the amplitude of the acoustic strain pulse arising from the heating of the SL is very small, on the order of 0.001%, in comparison with the 0.7% peak strain of the acoustic strain from the SRO layer. An acoustic pulse is also generated by the stress due to depolarization field screening in the layers. The stress profile resulting from depolarization-field screening, for example in the development of an acoustic pulse in $BiFeO_3$.[33] The pulse due to the depolarization field screening, on the order of 0.01%, is also far smaller than the amplitude of the acoustic strain pulse from the SRO layer. The distortion in the interval in which the acoustic pulse propagation occurs (0-64 ps) is thus dominated by the pulse generated by the heating of the SRO.

The acoustic pulse from the SRO bottom electrode propagates through the total thickness of the SL in time $\tau = d/v_{SL} = 32$ ps, where $v_{SL}$ is the longitudinal acoustic sound velocity in the SL. The acoustic perturbation is observed up to time $t = 2\,\tau$ in Figure 2 because the acoustic pulse from the SRO bottom electrode is reflected at the SL/air interface at $t = \tau$ and then propagates toward the SL/SRO interface. The high acoustic impedance mismatch at the SL/air interface causes the acoustic pulse to be reflected from the free surface with a 180° phase change.[34] After $2\tau = 64$ ps, the strain pulse reaches the SL/SRO interface and propagates through the SRO into the substrate. The low acoustic impedance mismatch at the SL/SRO and SRO/STO interfaces causes only 20% of the acoustic amplitude to be reflected towards the surface, as described in more detail in the Supporting Information.

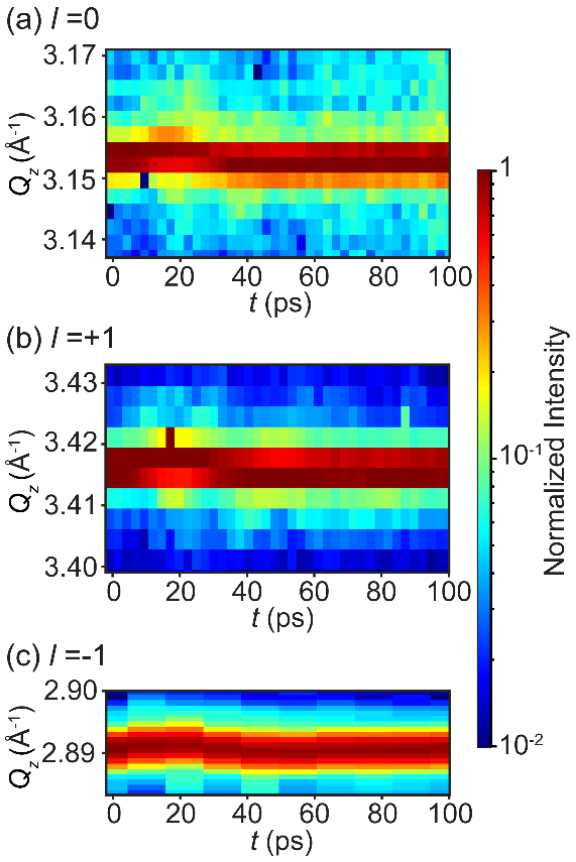


**Figure 2.** Scattered x-ray intensity as a function of $Q_z$ and time $t$ following optical excitation at $t$=0 for the **a)** $l$=0 SL 002 Bragg reflection and **b)** $l$=+1 and **c)** $l$=-1 SL satellite reflections near the 002 Bragg reflection. The intensity of each reflection is normalized to its peak value at $t < 0$.

The wavevectors of the maximum intensity for each reflection, $Q_{z,max}(l)$, vary as a function of $t$. The temporal variations of $Q_{z,max}(l)$ with $t$ for $l$=0,+1, and -1 reflections were extracted by fitting the peak profiles at each time step in the intensity maps in Figure 2 and are shown in **Figure 3**. The propagation of acoustic strain pulse to the surface and back to SL/SRO interface between 0 and 64 ps is responsible for the large variations in $Q_{z,max}(l)$ in this time regime. After 64 ps, $Q_{z,max}(l)$ maintains a lower value for the full-time range of the experiment, indicating that there is a photoinduced expansion that persists after the acoustic propagation is complete. The expansion in

the 64-100 ps time regime can be unambiguously separated from thermal expansion because the BTO/CTO SL shows thermal contraction in the 25-100 °C temperature regime, as described in the Supporting Information.

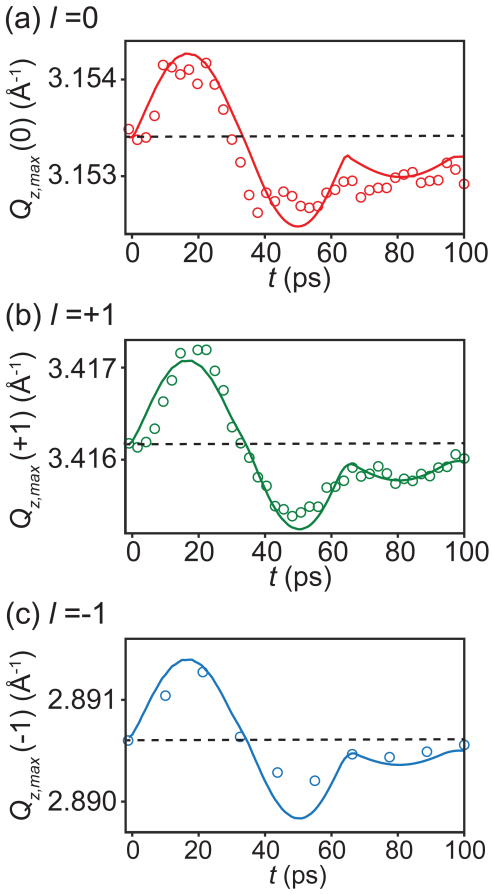


**Figure 3**. Measured (points) and simulated (solid line) time dependence of $Q_{z,max}(l)$ for **a)** BTO/CTO 002 Bragg reflection, $l$=0, and the **b)** SL $l$=+1 and **c)** SL $l$=-1 reflections near the BTO/CTO 002 reflection. The dashed lines indicate the steady-state values of $Q_{z,max}(l)$.

A comparison of the experimental results with an x-ray scattering simulation provides further insight into the structural distortion within the component layers. The atomic arrangement considered in the simulation consisted of an idealized BTO/CTO SL with time- and depth-dependent strain imposed by the acoustic pulse, depolarization field screening driven expansion,

and heating of SL. The diffracted intensity was calculated at each experimental time step using x-ray kinematical diffraction calculations. The initial atomic positions were set to provide equal ionic polarization in the BTO and CTO layers.

The strain imposed in the simulation consisted of the sum of the strain from the acoustic pulse, heating, and $\varepsilon_{net,depolarization}$, the depolarization field screening driven average strain in the SL. The strain $\varepsilon_{net,depolarization}$ was further decomposed into the lattice distortion of the BTO and CTO components using $\varepsilon_{BTO,depolarization}$ and $\varepsilon_{CTO,depolariation}$, the out-of-plane component $\varepsilon_{33}$ of the strain tensor in the BTO and CTO layers of the superlattice, respectively. In terms of these components, the net strain is given by $\varepsilon_{net,depolarization}=\frac{1}{6}(2\ \varepsilon_{BTO,depolarization} + 4\ \varepsilon_{CTO,depolarization})$. The values of $\varepsilon_{BTO,depolarization}$ and $\varepsilon_{CTO,depolarization}$ were separately determined by comparing the experimental data with the intensity predicted by the diffraction simulation. The ratio of the depolarization-field-screening driven distortions of the two components is $r = \frac{4\ \varepsilon_{CTO,depolarization}}{2\ \varepsilon_{BTO,depolarization}}$.

The values of $Q_{z,max}(l)$ were extracted from the simulated kinematical diffraction patterns for $l$=0, +1, and -1 at each time step and compared to the experimentally observed time dependence of $Q_{z,max}(l)$. Simulations with $\varepsilon_{net,depolarization}$=0.007 (±0.002)% agree with the experimental time dependence of $Q_{z,max}(l)$ for $l$=0,+1, and -1 and are plotted as solid lines in Figure 3a-c. The simulated variation of $Q_{z,max}(l)$ does not depend on the value of $r$. The simulations include the strain pulse launched due to optical absorption in the SRO layer with a magnitude of 0.7%. The depolarization-field screening driven strain $\varepsilon_{net,depolarization}$ is thus orders of magnitude less than the peak magnitude of the strain pulse from the SRO. The two contributions, the amplitude of the acoustic strain pulse and the depolarization-field-drive strain, have their origins in different layers

of the heterostructure (i.e. the SL and SRO) and there is thus no physical significance in their relative magnitudes.

The experimentally observed variation of the diffracted intensity was used to determine the value of $r$ and thus to find the component-specific contributions to the depolarization-field-driven strain, $\varepsilon_{BTO,depolarization}$ and $\varepsilon_{CTO,depolariation}$. The time dependence of the integrated intensities of the $l$=0, +1, and -1 reflections are shown in **Figure 4**. The intensity of each reflection is normalized to its value at $t$<0. The intensities vary rapidly during the acoustic pulse propagation, between $t$=0 and 64 ps. The intensity does not, however, return to its initial value after the acoustic pulses have propagated into the substrate at $t$ > 64 ps. Simulated kinematical diffraction patterns with $\varepsilon_{net,depolarization}$=0.007 (±0.002)%, taken from the variation in $Q_{z,max}(l)$ in Figure 3, and $r$=-0.5 (±0.2) agree with the experimental data and are shown as solid lines in Figure 4a-c. The variation of the goodness of fit for different values of $\varepsilon_{net,depolarization}$ and $r$ and the determination of the uncertainty in these parameters are described in the Supporting Information.

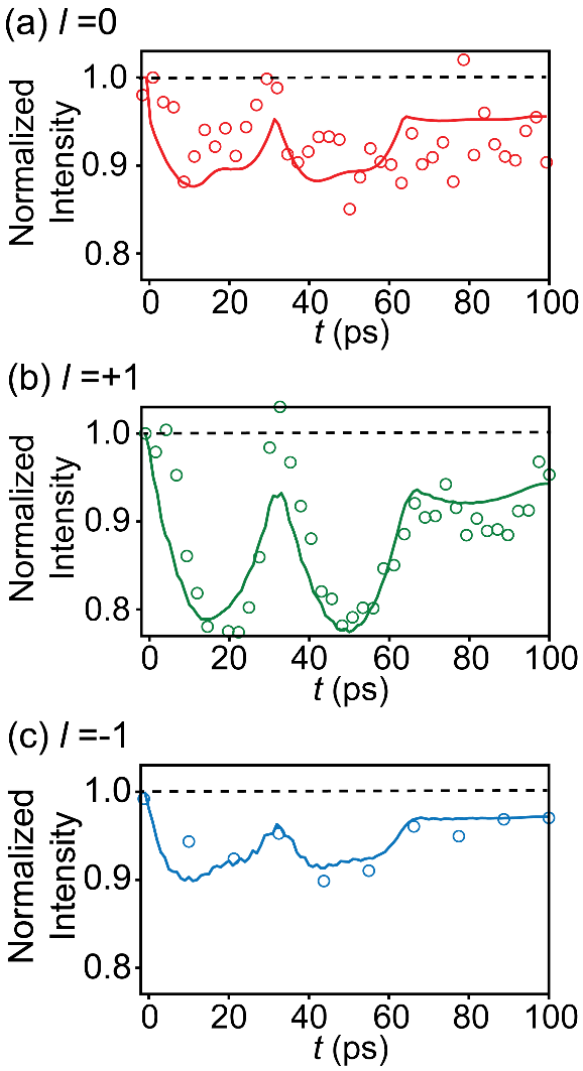


**Figure 4.** Time dependence of the measured (points) and simulated (solid lines) diffracted x-ray intensity for the **a)** BTO/CTO 002 Bragg reflection, $l$=0, and the **b)** SL $l$=+1 and **c)** SL $l$=-1 reflections near the BTO/CTO 002 reflection. The intensity of each reflection is normalized to its value at $t < 0$.

The negative value of $r$ obtained from the intensity data in Figure 4 indicates that depolarization field screening produces opposite strains in BTO and CTO layers. In BTO thin films, screening of the depolarization field leads to an increase in the polarization of the BTO

layers and hence the BTO layers have expansive strain.[9] A similar effect likely applies to superlattices, and we thus expect $\varepsilon_{BTO,depolarization}$ to be positive. The negative value of $r$ then indicates that there is a photoinduced compressive strain in the CTO layers. The fitted values of $\varepsilon_{net,depolarization}$= 0.007% and $r$ =-0.5 from Figures 3 and 4 give $\varepsilon_{BTO,depolarization}$ = 0.04% and $\varepsilon_{CTO,depolarization}$ = -0.01%.

In the LGD theory description, the relationship between the lattice parameter $c_i$ and polarization $P_i$ of layer $i$ is $P_i^2 \propto \frac{c_i}{a} - 1$.[13] With this approximation, the net change in polarization due to the optical excitation can be calculated from the values of $\varepsilon_{net,depolarization}$ and $r$. The in-plane lattice parameter $a$ is fixed by the epitaxial synthesis of the SL on the STO substrate, $a$=3.905 Å. The fractional change in the polarization of each component can be approximated as $\frac{\Delta P_i}{P_i} = \frac{1}{2}\varepsilon_i\left(\frac{c_{i,0}}{c_{i,0}-a}\right)$, where $c_{i,0}$ is the steady-state out-of-plane lattice parameter of component $i$ (see Supporting Information). The values of the steady-state out-of-plane lattice parameter of each component layer are assumed to be equal to the average lattice parameter of the SL measured from the 002 SL Bragg reflection at $l$=0, $c_{BTO,0} = c_{CTO,0}$ = 3.985 Å. This approach with the experimental results $\varepsilon_{net,depolarization}$= 0.007 (±0.002)% and $r$ = -0.5 (±0.2) give $\Delta P_{BTO}/P_{BTO}$= 2% and $\Delta P_{CTO}/P_{CTO}$ = -1%. The small fractional change in the polarization of BTO layers indicates that there is a partial screening of the depolarization field in BTO layers. Diffraction studies in an applied electric field indicated that the BTO and CTO components have equal piezoelectric strain.[26] The difference between the magnitudes of $\Delta P_{BTO}$ and $\Delta P_{CTO}$ is thus an intriguing result because screening of the depolarization field should normally be expected to create equal and opposite changes in the polarization and the strain in the two layers. The origin of the difference may arise from other contributions to the polarization of the CTO layers in SLs, including a reduction in the antipolar

rotation of CTO oxygen octahedra in the at the BTO/CTO interface in comparison with bulk CTO.[17, 27-28]

The oxygen octahedral rotation is suppressed in the CTO layers near the BTO/CTO interfaces because BTO strongly resists oxygen octahedral rotation.[17, 27] The photoexcited charge carriers are not expected to affect the polarization contribution arising from the octahedral rotation suppression. Hence, the lattice contraction and corresponding polarization reduction in the CTO layers are smaller in magnitude compared to that of the BTO layers. The suppression of oxygen octahedral rotation, however, favors the polarization in [111] direction in the CTO layers, similar to $BiFeO_3$.[17] The complete compensation of the depolarization field in the BTO layers would nullify the contribution of the BTO polarization to the polarization of CTO layers along [001] direction. Therefore, if optical excitation with sufficiently high fluence to screen the depolarization field fully in the BTO were possible, a distinct metastable polarization configuration in the CTO layers could be produced. In the case of complete screening the CTO polarization would be dominated only by strain and octahedral rotation effects.

**Conclusion**

The ultrafast response of BTO/CTO SLs to an above-bandgap optical pulse produces strain in each component layer. The screening of the depolarization field in the SL results in a reduction in the magnitude of the internal electric field in the CTO and leaves the CTO layers with reduced polarization. An analysis of photoinduced strain shows that the depolarization field screening in the SL leads to a 2% increase in the polarization of BTO layers and a reduction of 1% in the polarization of CTO layers. The case of optical excitation is completely different than an applied electric field, as when the SL is incorporated in a thin-film capacitor. An applied electric field

leads to piezoelectric expansion in both the BTO and CTO components, as expected from the equal steady-state polarization of these layers.[26] Optical excitation leads instead to a reduction in the polarization and lattice parameter of CTO, providing a different and complementary approach for the systematic variation of the polarization of the DE layers. The reduction of the polarization in the CTO layers along the [001] direction through depolarization field screening opens up the possibility of attaining a metastable polarization in the CTO layers.

**Experimental Section**

The BTO/CTO SL heterostructure consisted of 80 periods of the BTO/CTO repeating unit, with a SL thickness of 191 nm, epitaxially grown on an (001)-oriented 5-nm thick SRO layer on a (001) STO substrate. The structural distortion resulting from above-bandgap optical excitation was probed at the XSS beamline of Pohang Accelerator Laboratory XFEL (PAL-XFEL), using the arrangement in Figure 1(a).[35] A 100 fs-duration π-polarized optical laser pump with 3.1 eV photon energy and optical fluence of 13.5 mJ $cm^{-2}$ was used to excite the SL. The x-ray pulses had a photon energy of 9.7 keV, 25 fs duration, and a repetition rate of 30 Hz. The x-ray fluence was selected to maintain the diffracted signal at an intensity within the dynamic range of the multi-port charge-coupled device x-ray detector and to be lower than the damage threshold previously measured for $BiFeO_3$ thin film layers under the same conditions.[36] The diffraction patterns corresponding to SL *l=0*, *l=+1* and, *l=-1* reflections near the 002 reflection were measured in the delay range -1 to 100 ps.

**Supporting Information**

Supporting Information is available from the Wiley Online Library or from the author.

**Acknowledgments**

The authors gratefully acknowledge support from the U.S. DOE, Basic Energy Sciences, Materials Sciences and Engineering Division, under contract no. DE-FG02-04ER46147. H.J.L. acknowledges support by the National Research Foundation of Korea under grant 2017R1A6A3A11030959. Y.J.A. acknowledges support from the National Science Foundation through grant number DMR-1609545. J.C. acknowledges support from the CNRS project GOtoXFEL. The authors acknowledge the use of characterization facilities supported by the National Science Foundation through the University of Wisconsin Materials Research Science and Engineering Center (DMR-1720415). The experiment was performed at the XSS beamline of PAL-XFEL (proposal no. 2018-2nd-XSS-016) funded by the Ministry of Science and ICT of Korea. The synthesis work at ORNL was supported by U.S. DOE, Basic Energy Sciences, Materials Sciences and Engineering Division.

**Conflict of Interest**

The authors declare no conflict of interest.

**Author Contributions**

D.S.G. and H.J.L. contributed equally to this work. H.J.L. and P.G.E. designed the experiments. H.J.L., Y.A., J.C., T.K., S.U., J.Y.L., S.H.C., S.K., I. E., M.K., S.Y.P., K.S.K., J.Y.J., and P.G.E. carried out the time-resolved free-electron-laser x-ray diffraction experiments. D.S.G. and H.J.L. analyzed the scattering data and developed the supporting calculations. H.N.L. synthesized the superlattice sample. D.S.G. and P.G.E wrote the manuscript. All authors contributed to the discussions and the revision of the manuscript.

**References**

[1] M. Dawber, E. Bousquet, *MRS Bull.* **2013**, 38, 1048.

[2] H. Wang, F. Tang, P. H. Dhuvad, X. Wu, *npj Comput. Mater.* **2020**, 6, 1.

[3] P. Zubko, N. Jecklin, A. Torres-Pardo, P. Aguado-Puente, A. Gloter, C. Lichtensteiger, J. Junquera, O. Stéphan, J.-M. Triscone, *Nano Lett.* **2012**, 12, 2846.

[4] D. Bennett, M. Muñoz-Basagoiti, E. Artacho, *Roy. Soc. Open Sci.* **2020**, 7, 201270.

[5] M. Sepliarsky, S. R. Phillpot, D. Wolf, M. G. Stachiotti, R. L. Migoni, *Phys. Rev. B* **2001**, 64, 060101.

[6] J. B. Neaton, K. M. Rabe, *Appl. Phys. Lett.* **2003**, 82, 1586.

[7] S. M. Nakhmanson, K. Rabe, D. Vanderbilt, *Phys. Rev. B* **2006**, 73, 060101.

[8] V. A. Stoica, N. Laanait, C. Dai, Z. Hong, Y. Yuan, Z. Zhang, S. Lei, M. R. McCarter, A. Yadav, A. R. Damodaran, *Nature Mater.* **2019**, 18, 377.

[9] Y. Ahn, A. S. Everhardt, H. J. Lee, J. Park, A. Pateras, S. Damerio, T. Zhou, A. D. DiChiara, H. Wen, B. Noheda, P. G. Evans, *Phys. Rev. Lett.* **2021**, 127, 097402.

[10] P. Zubko, N. Stucki, C. Lichtensteiger, J.-M. Triscone, *Phys. Rev. Lett.* **2010**, 104, 187601.

[11] Y. Ahn, J. Park, A. Pateras, M. B. Rich, Q. Zhang, P. Chen, M. H. Yusuf, H. Wen, M. Dawber, P. G. Evans, *Phys. Rev. Lett.* **2017**, 119, 057601.

[12] P. Chen, M. P. Cosgriff, Q. Zhang, S. J. Callori, B. W. Adams, E. M. Dufresne, M. Dawber, P. G. Evans, *Phys. Rev. Lett.* **2013**, 110, 047601.

[13] H. J. Lee, Y. Ahn, S. D. Marks, E. C. Landahl, S. Zhuang, M. H. Yusuf, M. Dawber, J. Lee, T. Kim, S. Unithrattil, S. H. Chun, S. Kim, I. Eom, S.-Y. Park, K. S. Kim, S. Lee, J. Y. Jo, J. Hu, P. G. Evans, *Phys. Rev. X* **2021**, 11, 031031.

[14] M. Dawber, C. Lichtensteiger, M. Cantoni, M. Veithen, P. Ghosez, K. Johnston, K. Rabe, J.-M. Triscone, *Phys. Rev. Lett.* **2005**, 95, 177601.

[15] F. A. Urtiev, V. G. Kukhar, N. A. Pertsev, *Appl. Phys. Lett.* **2007**, 90, 252910.

[16] E. Bousquet, M. Dawber, N. Stucki, C. Lichtensteiger, P. Hermet, S. Gariglio, J.-M. Triscone, P. Ghosez, *Nature* **2008**, 452, 732.

[17] H. Wang, J. Wen, D. J. Miller, Q. Zhou, M. Chen, H. N. Lee, K. M. Rabe, X. Wu, *Phys. Rev. X* **2016**, 6, 011027.

[18] S. Das, Y. L. Tang, Z. Hong, M. A. P. Gonçalves, M. R. McCarter, C. Klewe, K. X. Nguyen, F. Gómez-Ortiz, P. Shafer, E. Arenholz, *Nature* **2019**, 568, 368.

[19] A. K. Yadav, C. T. Nelson, S. L. Hsu, Z. Hong, J. D. Clarkson, C. M. Schlepütz, A. R. Damodaran, P. Shafer, E. Arenholz, L. R. Dedon, *Nature* **2016**, 530, 198.

[20] V. A. Stephanovich, I. A. Luk'yanchuk, M. G. Karkut, *Phys. Rev. Lett.* **2005**, 94, 047601.

[21] A. L. Roytburd, S. Zhong, S. P. Alpay, *Appl. Phys. Lett.* **2005**, 87, 092902.

[22] H. Wen, P. Chen, M. P. Cosgriff, D. A. Walko, J. H. Lee, C. Adamo, R. D. Schaller, J. F. Ihlefeld, E. M. Dufresne, D. G. Schlom, *Phys. Rev. Lett.* **2013**, 110, 037601.

[23] D. Daranciang, M. J. Highland, H. Wen, S. M. Young, N. C. Brandt, H. Y. Hwang, M. Vattilana, M. Nicoul, F. Quirin, J. Goodfellow, T. Qi, I. Grinberg, D. M. Fritz, M. Cammarata, D. Zhu, H. T. Lemke, D. A. Walko, E. M. Dufresne, Y. Li, J. Larsson, D. A. Reis, K. Sokolowski-Tinten, K. A. Nelson, A. M. Rappe, P. H. Fuoss, G. B. Stephenson, A. M. Lindenberg, *Phys. Rev. Lett.* **2012**, 108, 087601.

[24] R. M. Fleming, D. B. McWhan, A. C. Gossard, W. Wiegmann, R. A. Logan, *J. Appl. Phys.* **1980**, 51, 357.

[25] J. Y. Jo, R. J. Sichel, E. M. Dufresne, H. N. Lee, S. M. Nakhmanson, P. G. Evans, *Phys. Rev. B* **2010**, 82, 174116.

[26] J. Y. Jo, R. J. Sichel, H. N. Lee, S. M. Nakhmanson, E. M. Dufresne, P. G. Evans, *Phys. Rev. Lett.* **2010**, 104, 207601.

[27] X. Z. Lu, X. G. Gong, H. J. Xiang, *Comput. Mater. Sci.* **2014**, 91, 310.

[28] X. Wu, K. M. Rabe, D. Vanderbilt, *Phys. Rev. B* **2011**, 83, 020104.

[29] S. S. A. Seo, H. N. Lee, *Appl. Phys. Lett.* **2009**, 94, 232904.

[30] C.-J. Eklund, C. J. Fennie, K. M. Rabe, *Phys. Rev. B* **2009**, 79, 220101.

[31] D. A. Reis, M. F. DeCamp, P. H. Bucksbaum, R. Clarke, E. Dufresne, M. Hertlein, R.

Merlin, R. Falcone, H. Kapteyn, M. M. Murnane, *Phys. Rev. Lett.* **2001**, 86, 3072.

[32] C. Thomsen, H. T. Grahn, H. J. Maris, J. Tauc, *Phys. Rev. B* **1986**, 34, 4129.

[33] D. Schick, M. Herzog, H. Wen, P. Chen, C. Adamo, P. Gaal, D. G. Schlom, P. G. Evans, Y. Li, M. Bargheer, *Phys. Rev. Lett.* **2014**, 112, 097602.

[34] D. Schick, M. Herzog, A. Bojahr, W. Leitenberger, A. Hertwig, R. Shayduk, M. Bargheer, *Struct. Dyn.* **2014**, 1, 064501.

[35] H.-S. Kang, C.-K. Min, H. Heo, C. Kim, H. Yang, G. Kim, I. Nam, S. Y. Baek, H.-J. Choi, G. Mun, *Nature Photon.* **2017**, 11, 708.

[36] H. J. Lee, Y. Ahn, S. D. Marks, E. C. Landahl, J. Y. Lee, T. Y. Kim, S. Unithrattil, J. Y. Jo, S. H. Chun, S. Kim, S.-Y. Park, I. Eom, C. Adamo, D. G. Schlom, H. Wen, P. G. Evans, *Appl. Phys. Lett.* **2019**, 115, 252903.